RSC Advances

PAPER

View Article Online
View Journal | View Issue

Cite this: *RSC Adv.*, 2026, **16**, 28167

Theoretical investigation of electrochemical behavior of DTPA and its interfacial synergy with defected graphene toward photocatalytic applications

Chinh Dung Trinh,[ab] Thi Long Do,[c] Tam Van Nguyen,[d] Ngan Nguyen Le[ef] and Duong Nguyen Nguyen *[ef]

Received 2nd April 2026
Accepted 18th May 2026

DOI: 10.1039/d6ra02766k

rsc.li/rsc-advances

A comprehensive density functional theory (DFT) investigation is performed to elucidate the electrochemical behavior of diethylenetriaminepentaacetic acid (DTPA) and its interaction with defected graphene for photocatalytic applications. The calculations reveal that DTPA adopts a folded conformation stabilized by intramolecular hydrogen bonds. Upon oxidation, the molecule undergoes progressive hydrogen-bond weakening followed by C–C bond cleavage at higher charge states, whereas reduction induces a non-linear reorganization of the hydrogen-bond network without covalent bond breaking. Protonation and deprotonation substantially narrow the HOMO–LUMO gap, enabling visible-light photoactivity. Adsorption studies on graphene show that defect engineering, particularly the Stone–Wales defect, significantly enhances binding. A photocatalytic mechanism is proposed wherein DTPA serves as the hole source for water oxidation and defected graphene as the electron sink for oxygen reduction, providing a rational foundation for molecular–carbon hybrid photocatalysts.

1. Introduction

Diethylenetriaminepentaacetic acid (DTPA) is a well-known polyaminocarboxylic acid widely utilized in coordination chemistry, chelation therapy, and as a precursor for functional carbon materials.[1–5] Its chemical formula $C_{14}H_{23}N_3O_{10}$, comprises three tertiary amine nitrogen atoms and five carboxylic acid groups, giving it a high denticity and a remarkable ability to coordinate metal ions.[6,7] Structurally, DTPA adopts a compact, folded conformation stabilized by a network of intramolecular hydrogen bonds, which pre-organize the functional groups and reduce conformational flexibility. This preorganization is a key factor in its exceptional chelating efficiency and selectivity toward lanthanides, actinides, and transition metals.[8–10]

Owing to its strong metal-binding capacity, DTPA has found widespread application in diverse fields. Its primary uses include chelation therapy for the removal of toxic heavy metals such as plutonium, americium, and lead from the human body,[11,12] and as a contrast agent carrier in magnetic resonance imaging (MRI) when complexed with gadolinium.[13,14] In environmental chemistry, DTPA is employed for soil decontamination and for the mobilization of radionuclides in nuclear waste treatment.[15] Beyond these well-established applications, DTPA serves as a versatile building block for functional materials. It has been used as a precursor for nitrogen-doped porous carbons, which exhibit excellent performance in supercapacitors and electrocatalysis,[16,17] and as a linker in metal–organic frameworks (MOFs) with tunable porosity and catalytic activity.[18,19] More recently, DTPA has gained attention in the field of photocatalysis, where it acts as a molecular active site when immobilized on conductive carbon supports, facilitating hydrogen peroxide production *via* two-electron oxygen reduction.[20]

Despite its widespread use, the fundamental electrochemical behavior of DTPA remains incompletely characterized. In its metal complexes, the redox activity is often dominated by the metal center, masking the intrinsic properties of the ligand.[21] As a free molecule, DTPA can undergo sequential electron–transfer reactions, giving rise to radical cationic and anionic states that are expected to display distinct structural reorganizations. However, experimental isolation and characterization of these

[a]*Laboratory of Advanced Materials Chemistry, Institute for Advanced Study in Technology, Ton Duc Thang University, Ho Chi Minh City, Vietnam*

[b]*Faculty of Applied Sciences, Ton Duc Thang University, Ho Chi Minh City, Vietnam*

[c]*Faculty of Chemical Engineering, Industrial University of Ho Chi Minh City, Ho Chi Minh City, Vietnam*

[d]*Institute of Advanced Technology and Artificial Intelligence, Hung Vuong University of Ho Chi Minh City, Vietnam*

[e]*Institute of Applied Science and Technology, Van Lang School of Technology, Van Lang University, Ho Chi Minh City, Vietnam. E-mail: nguyen.nd@vlu.edu.vn; Tel: +84 798 740 848*

[f]*Faculty of Applied Technology, Van Lang School of Technology, Van Lang University, Ho Chi Minh City, Vietnam*

charged states are challenging due to their short lifetimes and the difficulty of controlling the protonation equilibria that accompany electron transfer.[22] Consequently, the relationship between the molecular structure of DTPA and its electrochemical response, particularly how the hydrogen-bonding network accommodates excess charge, remains largely speculative. From a materials perspective, the ability of DTPA to engage in strong non-covalent interactions makes it an attractive candidate for constructing hybrid systems. Experimentally, DTPA has been shown to act as a stable redox-active component in photogalvanic cells[23] and as a recyclable molecular scaffold in photocatalytic systems.[24] Recent experimental work on a DTPA-based hybrid (denoted DG5) demonstrated exceptional photocatalytic activity for hydrogen peroxide synthesis, outperforming most reported metal-free photocatalysts.[20] However, that investigation focused on material synthesis and macroscopic performance, leaving the atomic-level mechanisms—such as the preferred adsorption configuration of DTPA, the role of graphene defects, and the alignment of frontier orbitals—largely unexplored. While previous theoretical studies have examined graphene-supported clusters, these typically involve metal-containing inorganic active sites (*e.g.*, TiO_2).[25] Therefore, a systematic computational study is necessary to elucidate the intrinsic electrochemical behavior of DTPA and its interfacial synergy with defected graphene. To the best of our knowledge, this is the first theoretical work to map the redox landscape of free DTPA and quantify the role of graphene defects in anchoring the molecule for visible-light photocatalysis.

In this work, we employ density functional theory (DFT) to systematically unravel the intrinsic electrochemical properties of DTPA and to elucidate how its molecular structure responds to electron transfer, protonation, and interfacial interactions. The oxidized and reduced species of DTPA, including radical cation and anion states, formed upon one-electron oxidation and reduction was investigated. Turning to the hybrid interface, we assess the adsorption of DTPA on pristine, Stone–Wales (SW)-defected, and single-vacancy (V_1) defected graphene. Our results demonstrate that defect engineering significantly enhances binding affinity, with the SW defect providing the strongest interaction, thereby establishing a clear link between support structure and molecular anchoring. By aligning the frontier orbitals of DTPA with defected graphene, a photocatalytic mechanism is proposed in which DTPA serves as the photoactive center that generates holes for water oxidation, while the graphene support efficiently accepts electrons for oxygen reduction. This study fills a critical knowledge gap by providing a detailed TD-DFT analysis of the DTPA@graphene interface. By correlating calculated adsorption energies and interfacial charge transfer (ICT) profiles with reported experimental data such as RRDE and TPV, this work offers new mechanistic insights into the synergy between molecular active sites and defect-engineered carbon matrices. These findings provide a comprehensive atomic-level understanding of DTPA redox behavior and its synergy with carbonaceous supports, offering a rational foundation for the design of next-generation molecular–carbon hybrid photocatalysts.

2. Calculation details

All density functional theory (DFT) calculations were performed using the ORCA 6.1 program package.[26–28] The geometry optimizations and electronic structure analyses were carried out using the hybrid B3LYP functional, which combines Becke's three-parameter exchange functional with the Lee–Yang–Parr correlation functional. The def2-TZVP basis set was employed for all atoms, providing a balanced description of both valence and polarization effects. To account for long-range dispersion interactions, the D3 empirical correction of Grimme was applied. The self-consistent field (SCF) convergence criterion was set to 10^{-8} Eh, and geometry optimizations were considered converged when the maximum force component fell below 0.00045 Eh $bohr^{-1}$ and the displacement below 0.0018 bohr. Vibrational frequency analyses were conducted at the same level of theory to verify the nature of all stationary points. The absence of imaginary frequencies ($N_{imag} = 0$) for all optimized geometries confirms that they represent true local minima on the potential energy surface. Spin contamination was assessed by computing $\langle S^2 \rangle$ for all open-shell species (see Table S1 in the Supporting Information). For doublet states, the calculated $\langle S^2 \rangle$ values deviate from the ideal value of 0.75 by less than 10%, while the singlet states exhibit $\langle S^2 \rangle = 0.00$.

Solvent effects were modeled using the conductor-like polarizable continuum model (CPCM) with the default radii and dielectric constants implemented in ORCA for water, ethanol, *N*,*N*-dimethylformamide (DMF), and acetonitrile. For each solvent, the solvation free energy was decomposed into electrostatic, cavitation, dispersion, and outlying charge contributions. Single-point energy calculations in solution using the CPCM model were performed on the gas-phase optimized geometries to maintain consistency across all solvent conditions. For the study of DTPA adsorption on graphene substrates, a cluster model approach was adopted. During the geometry optimization process, all atomic coordinates for both the adsorbates and the graphene supports were fully relaxed until the force convergence criteria were met.The graphene sheets (pristine, Stone–Wales defect, and single-vacancy defect) were represented by finite fragments terminated with hydrogen atoms to saturate dangling bonds.

The adsorption energy (E_{ads}) of DTPA on the graphene clusters was calculated as:

$$E_{ads} = E_{hybrid} - (E_{DTPA} + E_{graphene})$$

where E_{hybrid}, $E_{graphene}$, and E_{DTPA} represent the total energies of the hybrid system, the isolated graphene support, and the isolated DTPA ligand, respectively. To account for the Basis Set Superposition Error (BSSE), the counterpoise (CP) correction method was applied. The CP corrections were calculated at the single-point energy level using the geometries previously optimized without the correction. Spin density distributions, charge density differences, and density of states (DOS) were analyzed from the converged wavefunctions using Multiwfn software.

To evaluate the thermodynamic feasibility of sequential electron transfer from the neutral DTPA molecule to its cationic

and anionic states, the Gibbs free energy change (ΔG) for each half-reaction was estimated in aqueous solution. For a process $M \rightarrow M^{n+} + ne^-$ (oxidation) or $M + ne^- \rightarrow M^{n-}$ (reduction), ΔG was approximated as:

$$\Delta G \approx \Delta E_{\text{electronic}} + \Delta\text{ZPE} - T\Delta S$$

where $\Delta E_{\text{electronic}}$ is the difference in total electronic energies (including solvation from CPCM) between the charged state and the neutral molecule, ΔZPE is the difference in zero-point vibrational energies obtained from harmonic frequency calculations, and $T\Delta S$ is the entropy contribution at 298.15 K (approximated from vibrational, rotational, and translational degrees of freedom using standard statistical thermodynamics as implemented in ORCA). For the multi-electron steps ($n \geq 2$), ΔG was computed as the sum of successive one-electron ΔG values. The calculated absolute potentials were referenced to the Standard Hydrogen Electrode (SHE) using an absolute value of 4.44 V to allow direct comparison with experimental data.

To characterize the optical absorption properties of materials, time-dependent density functional theory (TD-DFT) calculations were performed. Herein, the range-separated hybrid functional CAM-B3LYP was employed, which is known to provide a more accurate description of charge-transfer excited states compared to conventional hybrids B3LYP. Solvent effects of water were included with the same parameters as in the ground-state calculations. The lowest 20 singlet–singlet vertical excitation energies were computed at the optimized ground-state geometry of the hybrid.

3. Result and discussion

3.1. Neutral state

Fig. 1a presents the fully optimized geometry of the DTPA molecule obtained from density functional theory (DFT) calculations. The structure adopts a compact, folded conformation stabilized by two prominent intramolecular hydrogen bonds that play a decisive role in organizing the molecular framework. In detail, an O–H···N contact of 1.959 Å links one carboxylic acid group to a central tertiary amine nitrogen, while an O–H···O interaction of 1.851 Å connects two adjacent carboxylic acid moieties. These moderately strong hydrogen bonds effectively lock the five carboxylic acid arms and three tertiary amine centers into a pre-organized arrangement, significantly reducing conformational flexibility and creating a spatially well-defined scaffold that is primed for intermolecular interactions.

Fig. 1b displays the electrostatic potential (ESP) map, pronounced complementarity of charge distribution arises naturally from the intramolecular hydrogen-bond network. The data provides an intuitive explanation for strong tendency of DTPA to form directed non-covalent contacts. Complementing both the structural and electrostatic insights, Fig. 1c illustrates the frontier molecular orbital energies of the isolated molecule. The highest occupied molecular orbital (HOMO) resides at −6.192 eV, primarily on the nitrogen lone pairs and adjacent carboxylate groups, while the lowest unoccupied molecular orbital (LUMO) is located at −0.781 eV and is dominated by the π^* antibonding orbitals of the carbonyl groups, resulting in a HOMO–LUMO gap of 5.411 eV that classifies free DTPA as a wide-bandgap species. Fig. 1 establishes the isolated DTPA as a reliable reference state, providing the essential baseline of geometric parameters, charge distribution, and orbital energetics required for all subsequent computational analyses of its electrochemical behavior in more complex chemical environments.

To complement the structural and electronic characterization of the isolated DTPA molecule, a quantitative assessment of molecular properties in various solvent is investigated (Table S2). Notably, the cavitation + dispersion term exhibits a sign change: it is positive for water and ethanol but negative for DMF and acetonitrile, indicating that the attractive dispersion interactions between DTPA and the less structured organic solvents outweigh the energetic cost of cavity formation. These trends highlight the sensitivity of DTPA electronic energy to the molecular environment, a factor that will influence its redox potentials and adsorption affinity. It should be noted that the static electric properties of DTPA are also significant in such solvents (Table S3).

3.2. Radical cation and anion

Fig. 2 expands the investigation from the neutral DTPA molecule to a series of progressively oxidized and reduced states. For each form, the optimized geometries are displayed alongside selected intramolecular hydrogen-bond lengths (in Å), allowing a direct comparison with the neutral reference and revealing how the molecular framework responds structurally to the incremental gain or loss of electrons. The cationic sequence begins with the removal of one electron to form the radical cation (Cation +1). At this stage, the molecule retains its overall folded architecture, but the intramolecular hydrogen bonds that stabilize the compact conformation undergo significant elongation relative to the neutral state. In detail, the O–H···O interaction between two adjacent carboxylic acid moieties lengthens to 2.358 Å, while the O–H···N contact linking a carboxylic acid to a tertiary amine nitrogen extends to 2.310 Å. Despite the weakening of hydrogen bonds, the molecule remains intact as a single covalently connected entity. A dramatic transformation occurs upon further oxidation to Cation +2: a central carbon–carbon bond undergoes cleavage, breaking the originally contiguous molecular backbone into two distinct fragments. Therein, they are held together exclusively by intermolecular hydrogen bonds. The figure annotates this hydrogen-bonded interface with a precise distance of 1.570 Å, indicating a remarkably strong interaction that compensates for the loss of the covalent linkage. This bond rupture represents a fundamental change in molecular connectivity: a "structural bifurcation" that is not observed in the neutral or singly charged cation. Upon one more electron removal to form Cation +3, the two-fragment architecture persists, but the hydrogen-bonded contact between the fragments adjusts to a slightly longer distance of 1.864 Å. The increase in bond length suggests that the additional positive charge modifies the charge distribution across the fragments, subtly weakening the

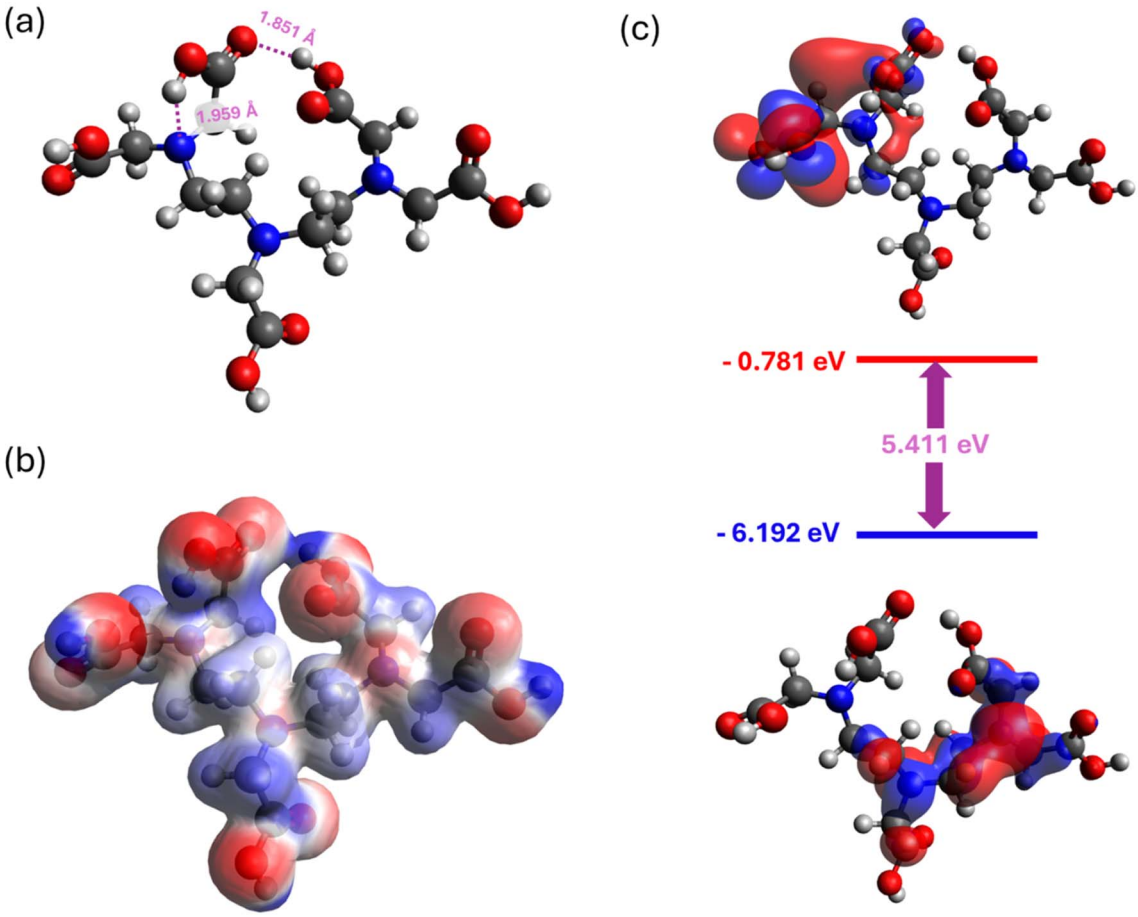

Fig. 1 (a) Optimized molecular structure of DTPA with key intramolecular hydrogen bond lengths (Å). (b) Electrostatic potential surface of DTPA. (c) Calculated frontier orbital energies (HOMO and LUMO) and HOMO–LUMO gap of the isolated DTPA molecule.

intermolecular interaction while still maintaining the overall assembly. The initial weakening of the intramolecular hydrogen bonds in Cation +1 (2.358 Å and 2.310 Å) thus serves as a critical precursor, destabilizing the folded architecture and rendering the molecule susceptible to the catastrophic bond break that follows.

In sharp contrast, the anionic sequence proceeds without any covalent bond cleavage, but instead exhibits a profound reorganization of the hydrogen-bond network. Upon single-electron reduction to the radical anion (Anion −1), the added electron populates π^* orbitals delocalized over the carbonyl groups, increasing the electron density on oxygen atoms and altering the local acidity of the carboxylic OH groups. This electronic perturbation triggers a conformational rearrangement. In detail, the O–H group that originally participated in the O–H···N bond of neutral state rotates away from the tertiary amine nitrogen and reorients to form a new hydrogen bond with a neighboring carboxylic acid moiety, giving rise to an O–H···O–H bond. For Anion −2, the figure annotates two hydrogen bonds with distances of 1.744 Å and 1.703 Å, both characteristic of the newly established carboxyl–carboxyl interactions. For the most highly reduced state, Anion −3, the hydrogen-bond network expands further to encompass interactions, with distances of 1.609 Å and 1.856 Å for carboxyl–carboxyl interaction, and 2.092 Å for carboxyl-backbone attraction. This dispersion suggests that as excess negative charge accumulates, the molecule optimizes its hydrogen-bonding pattern to delocalize the charge over multiple carboxylate groups, with some interactions becoming exceptionally strong while others are weakened to accommodate geometric constraints. The structural change of the cationic and anionic forms reveals two fundamentally different structural response mechanisms. Oxidation beyond the singly charged state triggers a catastrophic covalent bond rupture, fragmenting the molecule into two pieces that nevertheless remain associated *via* strong hydrogen bonds. Reduction, by contrast, preserves the covalent integrity of the backbone while inducing a heterogeneous and non-linear evolution of the hydrogen-bond network. These distinct pathways have profound implications for the electrochemical behavior of DTPA and its hybrid.

Table 1 summarizes the selected C–C bond lengths and relative energies of DTPA cations in vacuum and water. The C–C bond remains intact in Cation +1 but cleaves completely in Cation +2 and Cation +3, with bond lengths exceeding 4.3 Å regardless of the environment. Solvation reduces the formation energy of each cation by approximately 25% compared to

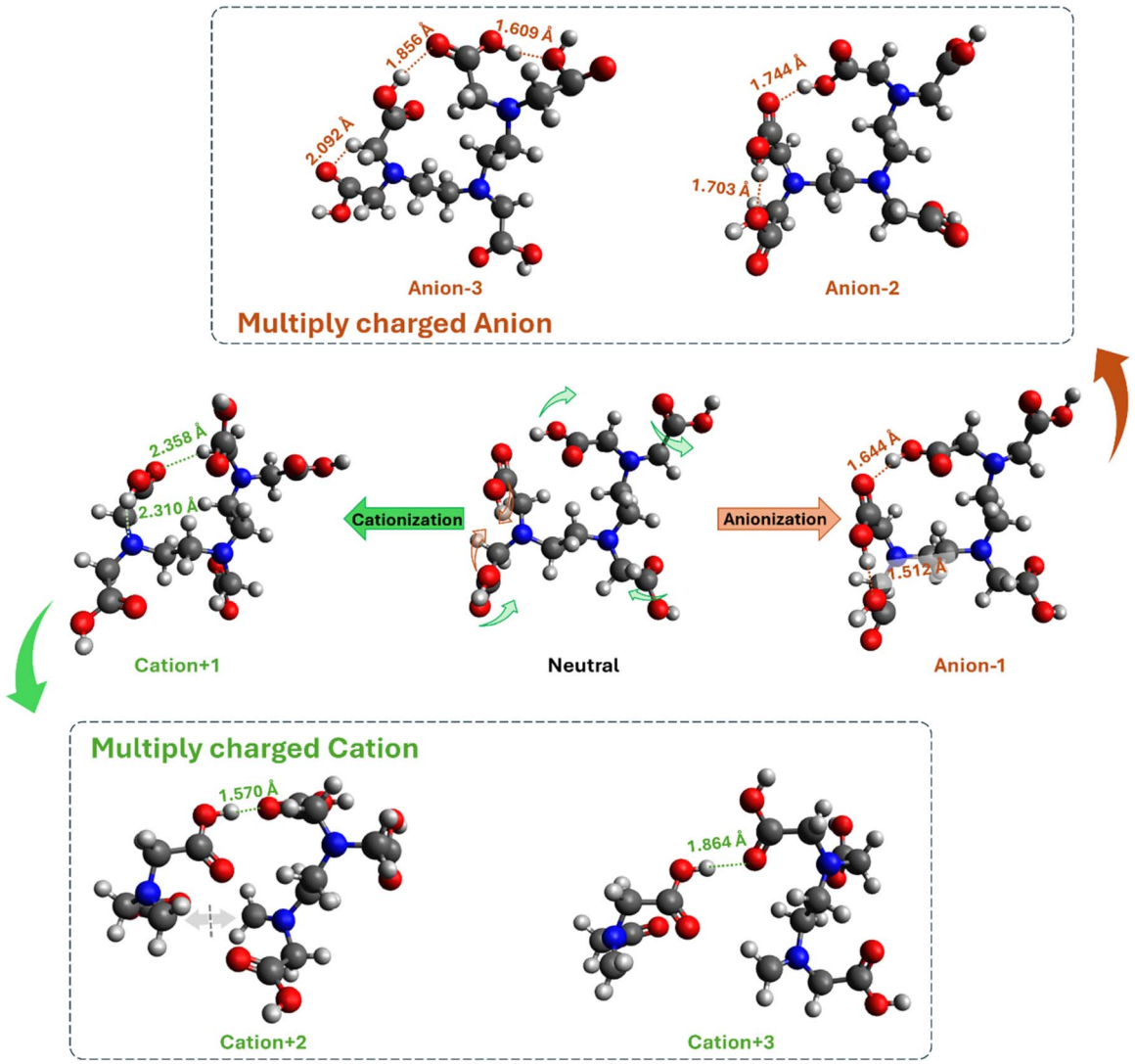

Fig. 2 Optimized geometries of DTPA in radical cationic and anionic states. Green arrows denote stepwise radical cationization (electron removal), and orange arrows denote stepwise radical anionization (electron addition). Key intramolecular hydrogen bond lengths (in Å) are indicated.

vacuum, but the energy cost for reaching Cation +2 (≥11.4 eV) or Cation +3 (≥21.0 eV) remains far above the photocatalytic potential window. These data confirm that the higher oxidation states are not accessible under mild photocatalytic conditions and serve only to define the intrinsic redox limits of DTPA.

Such observations offer a significant perspective on the electronic redistribution and thermodynamic stability associated with sequential electron removal or addition. Therefore, a correlation between the structural transformations and the changes in energetic-electronic properties relative to the neutral state was evaluated. Table 2 reports the calculated dipole moments and relative single point energies for each charged state, defined as the difference between the value of the cation/anion and that of the neutral molecule. Accordingly,

Table 1 C–C bond lengths and relative energies of DTPA cations in vacuum and water (CPCM)

State	ΔE (vacuum, eV)	C–C bond (vacuum, Å)	ΔE (water, eV)	C–C bond (water, Å)
Neutral	0	1.533	0	1.527
Cation +1	6.73	1.678	5.04	1.658
Cation +2	15.17	4.319	11.36	4.32
Cation +3	27.99	5.693	20.96	5.701

Table 2 Estimated Gibbs free energy changes (ΔG, eV) for sequential electron transfer steps of DTPA in water (CPCM) at 298.15 K[a]

Process	ΔG (eV)	Feasibility under photocatalysis	Explanation
Neutral → Cation +1	1.2	Yes	Hole generation
Cation +1 → Cation +2	6	No	Too uphill
Cation +2 → Cation +3	9.5	No	Chemically irrelevant
Neutral → Anion −1	−0.8	Yes	Electron reduction
Anion −1 → Anion −2	3.5	No	Inaccessible potential
Anion −2 → Anion −3	5	No	Structural limit only

[a] Entropic contributions ($T\Delta S$) are estimated to be within ±0.1 eV and are not explicitly included in the numbers above.

positive (or negative) values indicate an increase (or decrease) compared to the neutral reference.

The thermodynamic accessibility of the various charged states under photocatalytic conditions was evaluated by estimating the Gibbs free energy changes (ΔG) for sequential electron transfer steps in water, as summarized in Table 2. The one-electron oxidation (neutral → Cation +1) requires $\Delta G \approx$ +1.2 eV, while the one-electron reduction (neutral → Anion −1) is exergonic by $\Delta G \approx -0.8$ eV. Both values lie within the typical potential window of visible-light photocatalysis (*ca.* −1.0 V to +2.0 V *vs.* NHE at pH 7). In contrast, all second and third electron transfers (Cation +1 → Cation +2, Cation +2 → Cation +3, Anion −1 → Anion −2, and Anion −2 → Anion −3) require $\Delta G \geq 3.5$ eV in the uphill direction, making them impossible under mild photoexcitation conditions. These results justify focusing on the singly charged states (Cation +1 and Anion −1) as the relevant redox intermediates for the photocatalytic mechanism, while the higher charged states only serve to define the intrinsic redox limits of the DTPA backbone.

The susceptibility of DTPA anions to Proton-Coupled Electron Transfer (PCET) was evaluated through their proton affinity (PA) in the aqueous phase (Table S4). The significantly high PA values, particularly for the multi-anionic states, indicate a strong thermodynamic driving force for simultaneous proton capture following electron injection. This suggests that the stabilization of reduced DTPA species is not merely an electronic process but is intrinsically coupled with protonation, facilitating the overall photocatalytic pathway. Such high PA values confirm that DTPA effectively lowers the energy barrier for charge transfer by acting as a temporary proton-electron sink.

The changes in dipole moment ($\Delta\mu$) reported in Table 3 reflect the asymmetry of charge redistribution upon electron removal or addition. Anion −1 exhibits a remarkable enhancement in dipole moment by 9.48 debye relative to neutral, while Cation +1 shows a negligible decrease of −0.52 debye. This indicates that the hole is more symmetrically delocalized over the amine–carboxylate core, whereas the excess electron induces strong localization on one side of the molecule. For higher charged states, the dipole moments fluctuate, reflecting the complex structural distortions and fragment separations that accompany multi-electron processes. Regarding formation energy, removing one electron (Cation +1) raises the energy by 6.73 eV, while the second and third oxidations require an additional 8.43 eV and 12.82 eV, respectively. This progressive increase reflects both the growing coulombic penalty and the structural reorganization, particularly the bond cleavage in Cation +2 and Cation +3. For the anionic series, adding one electron (Anion −1) incurs a modest energy increase of only 0.20 eV, indicating that the neutral molecule readily accommodates an excess electron. Further reductions, however, become progressively more costly (3.70 eV for Anion −2 and 7.90 eV for Anion −3), consistent with the substantial hydrogen-bond reorganization and charge localization documented earlier. It should be noted that the changes for Cation +1 and Anion −1 in water environment are more significant than in vacuum (Table S5).

Fig. 3 provides a direct visualization of the unpaired electron distribution in the radical cation and radical anion of DTPA. It is evident that the transition between these states involves significant geometric distortions alongside changes in electron count. Upon cationization or anionization, the DTPA framework undergoes conformational relaxation, where the carboxylate arms and nitrogen lone pairs reorient to stabilize the net charge. The neutral molecule, as expected, exhibits no spin density, serving as a blank reference that underscores the absence of unpaired electrons. In contrast, both charged radical states display well-defined spin density distributions that reflect the distinct ways in which the molecule accommodates a hole (radical cation) *versus* an excess electron (radical anion). For the radical cation, the spin density is predominantly localized on the tertiary amine nitrogen atoms and the adjacent carboxylate groups. In the *XY* plane view, the isosurface appears

Table 3 Change in dipole moment (Debye) and relative single point energies (eV) of the radical cationic and anionic states of DTPA with respect to the neutral molecule

	Dipole moment[a] (debye)	Single point energy (eV)
Anion −1	9.48	0.20
Anion −2	2.13	3.70
Anion −3	5.78	7.90
Cation +1	−0.52	6.73
Cation +2	5.91	15.17
Cation +3	1.02	27.99

[a] Relative to the neutral molecule (absolute dipole moment of neutral = 4.79 debye).

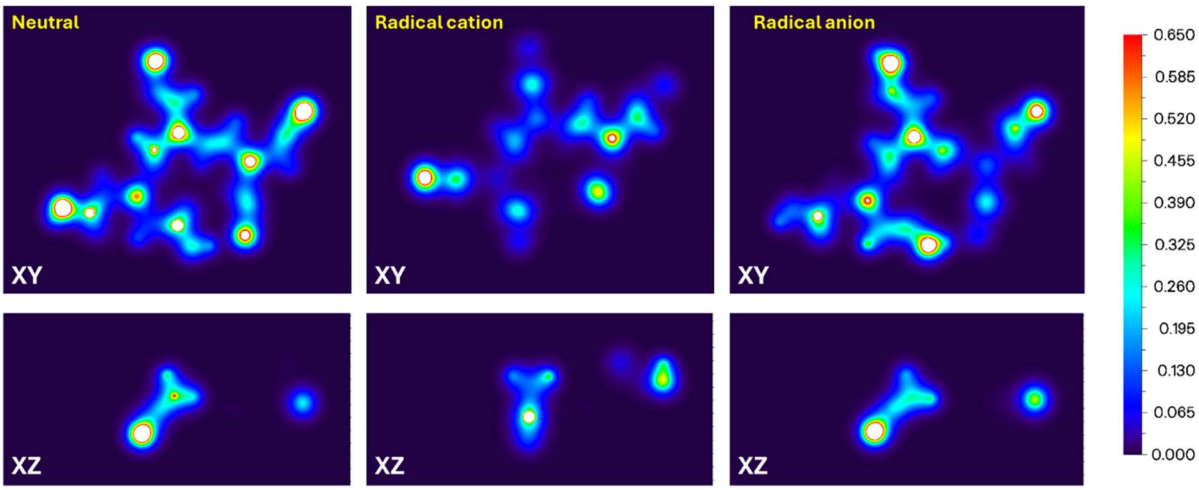

Fig. 3 Spin density isosurface maps of DTPA in (left) neutral, (middle) radical cationic, and (right) radical anionic forms. Upper panels correspond to the *XY* plane and lower panels to the *XZ* plane. The color bar indicates the magnitude of spin density (in a.u).

concentrated around the central region of the folded scaffold, with appreciable extension toward the carboxylic acid arms. The *XZ* plane further reveals that the spin density occupies a roughly planar arrangement, consistent with the removal of an electron from a molecular orbital that involves the lone pairs of the amine nitrogens and the π system of the neighboring carbonyl groups. The radical anion presents a markedly different spin density topology. Herein, the unpaired electron is almost exclusively confined to the carbonyl oxygen atoms of the carboxylic acid groups, with negligible density on the amine nitrogens. The *XY* plane shows distinct lobes of spin density projecting outward from the carboxyl moieties, while the *XZ* plane confirms that the excess electron resides in π* orbitals oriented perpendicular to the molecular plane. This localization is a direct electronic consequence of the additional electron populating the low-lying π* antibonding orbitals of the carbonyl groups, a feature already anticipated by the LUMO composition of the neutral molecule.

Fig. 4 presents charge density difference (CDD) plots that dissect the electron density redistribution accompanying the formation of the radical cation and radical anion of DTPA. The CDD maps were generated using a fixed-geometry (vertical) subtraction protocol to elucidate the initial sites of charge redistribution. For any transition between state A and state B, the CDD ($\Delta\rho$) is defined as $\rho_B(\text{geom}_A) - \rho_A(\text{geom}_A)$. This approach ensures that the observed density fluctuations strictly represent electronic gains or losses at specific atomic centers, providing a clear map of the 'active' regions for electron/hole localization. Comparing to the spin density maps, which locate the unpaired electron, the CDD analysis reveals the complete reorganization of electron density—both the electrons that are added or removed and the subsequent polarization of the remaining electron cloud. Fig. 4a depicts the electron density changes upon one-electron oxidation from the neutral molecule to the radical cation. The most prominent feature is a region of pronounced charge depletion localized around the tertiary amine nitrogen, corresponding to the removal of an electron from the HOMO. This accumulation reflects a subtle polarization of the remaining electron density in response to the hole, as the electron cloud reorganizes to partially compensate for the positive charge. Fig. 4b illustrates the opposite process: one-electron reduction from the neutral molecule to the radical anion. Herein, the dominant feature is a pronounced charge accumulation concentrated on the carbonyl oxygen atoms of the carboxylic acid groups. This localization is entirely consistent with the LUMO composition, which is dominated by π* antibonding orbitals of the carbonyl moieties, and with the spin density distribution, where the unpaired electron in the radical anion is confined to the same oxygen sites. In addition, the depletion signals the incipient reorganization of the hydrogen-bond network: as the added electron populates the carbonyl π* orbitals, the electron density on the O–H bonds decreases, weakening their proton-donating capacity and priming the structural rearrangement observed above, where the O–H group rotates away from the tertiary amine nitrogen to form a new O–H···O–H interaction with a neighboring carboxyl group.

Fig. 4c and d present the reverse processes—reduction of the radical cation back to neutral and oxidation of the radical anion back to neutral, respectively. In Fig. 4c, the conversion of the radical cation to neutral results in charge accumulation at the amine that was previously depleted, while the polarization effects along the hydrogen bonds are reversed. Similarly, Fig. 4d shows that returning the radical anion to neutral involves charge depletion from the carbonyl oxygens. The symmetry between the forward and reverse processes is a hallmark of the computational approach, confirming that the calculated charge redistributions are internally consistent and that the transformations are electronically reversible.

Fig. 5 presents the density of states (DOS) analysis for DTPA across its neutral, radical cation, and radical anion states, along with the corresponding reverse processes (cation-to-neutral and anion-to-neutral). For each state, the total DOS (TDOS) is shown in black, while the projected DOS (PDOS) contributions from

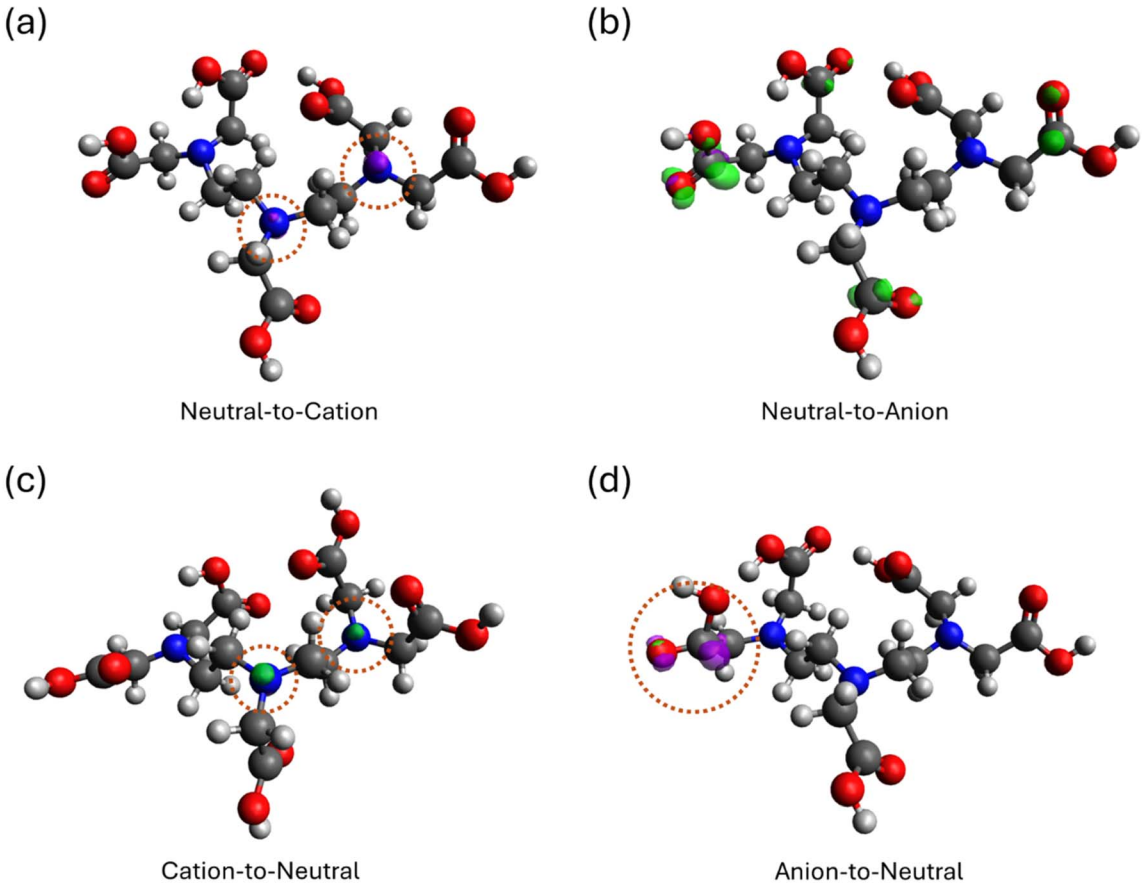

Fig. 4 Vertical charge density difference (CDD) plots illustrating electron density redistribution in DTPA upon radical cationization and anionization. (a) Neutral to radical cation, (b) neutral to radical anion, (c) radical cation to neutral, and (d) radical anion to neutral. Green isosurfaces indicate charge accumulation (positive), and purple isosurfaces indicate charge depletion (negative). Dashed circles mark the primary sites of charge variation.

the nitrogen atoms (cation-relative case) and the carbonyl oxygen atoms (anion-relative case) are overlaid to reveal the orbital origins of the frontier electronic structure. To quantify the impact of charge transfer on the electronic structure, we introduced a shift parameter, Δ, which represents the numerical deviation of the actual calculated energy level from this theoretical baseline. Such values were obtained by directly subtracting the Kohn–Sham orbital energies of the neutral molecule from those of the optimized charged species at the same level of theory. A positive Δ indicates an upward energy shift, while a negative value signifies a downward displacement, reflecting the electronic response of the system to the altered charge state.

The radical cationization sequence begins with the neutral molecule, whose TDOS exhibits a clear HOMO–LUMO gap consistent with the value reported above. Upon removal of one electron to form the radical cation, the electronic structure undergoes a characteristic reorganization. The most striking feature is the emergence of a new occupied state just below the Fermi level, which corresponds to the singly occupied molecular orbital (SOMO) of the radical cation. This SOMO is derived predominantly from the neutral HOMO, as evidenced by the strong nitrogen PDOS contribution. The Δ value annotated for this process quantifies the energy level alignment deviation: it represents the shift of the new state relative to either VBM or CBM of the neutral baseline. As shown in Fig. 5a, the actual energy level is shifted upward by $\Delta = +0.44$ eV (for neutral-to-cation) compared to the theoretical position of the neutral VBM. This indicates that the system experiences an energetic destabilization during the instantaneous electronic transition. Further structural relaxing to the cation state, the shift reaches $\Delta = +0.62$ eV. Upon reversal (cation-to-neutral), the DOS returns toward its neutral profile, with a shift of $\Delta = +0.36$ eV in comparing CBM level, reflecting the electronic reorganization energy required to restore the closed-shell configuration. Compared to the neutral molecule, the radical cation exhibits a significantly deeper SOMO and a lower-lying LUMO (Fig. S1), reflecting the enhanced electrostatic attraction of the electron cloud toward the positively charged molecular core.

The radical anionization sequence reveals a markedly different electronic response. Upon addition of one electron to form the radical anion, the new state is almost exclusively derived from the carbonyl PDOS, reflecting the LUMO composition of the neutral molecule. The Δ value for the anionization

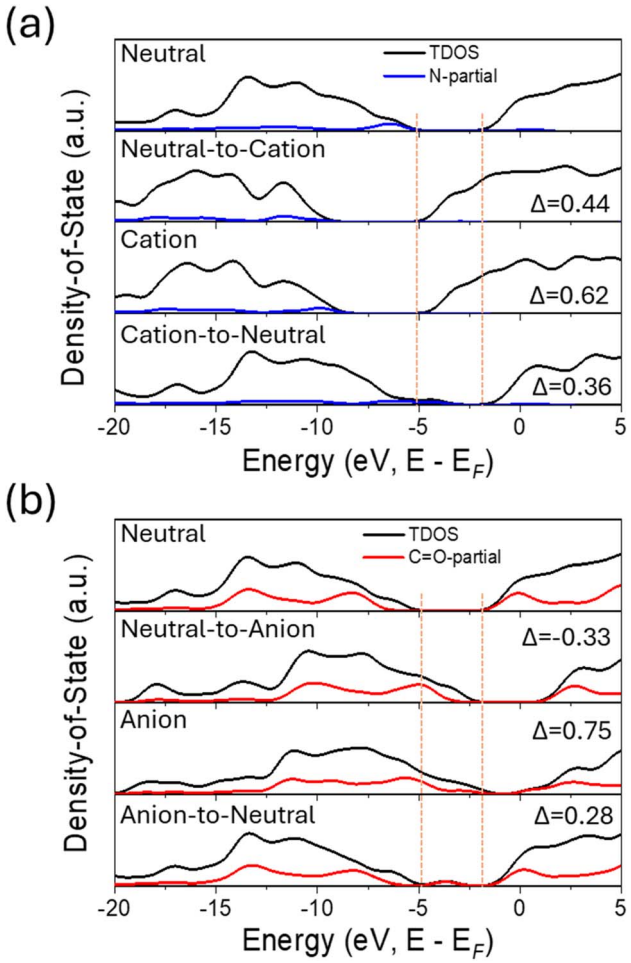

Fig. 5 Density of states (DOS) plots of DTPA upon radical (a) cationization and (b) anionization with total DOS (black), *N*-projected DOS (blue), and C=O-projected DOS (red) for neutral, cation/anion, and the reversible processes. The Δ values quantify the energy shift of the cationization ($HOMO_{neutral} \leftrightarrow SOMO_{cation}$) or anionization ($LUMO_{neutral} \leftrightarrow SOMO_{anion}$) relative to the neutral molecule. All energies are referenced to the Fermi level ($E_F = 0$).

process is annotated as $\Delta = -0.33$ eV, indicating that the actual level resides below the theoretical neutral CBM baseline. This downward shift reflects the energetic stabilization of the excess electron within the molecular framework. However, in the fully relaxed anion state, the $\Delta = +0.75$ eV shift indicates a significant destabilization, arising from the strong electron–electron repulsion and the accompanying structural reorganization documented in Fig. 2, where the hydrogen-bond network reconfigures to accommodate the excess charge. These Δ values effectively quantify the real-world deviation of the frontier orbitals from the idealized frozen-orbital positions during the redox cycle. Compared to the neutral molecule, the radical anion exhibits a significant upward shift of both frontier levels, with the SOMO residing above the Fermi level (Fig. S2).

3.3. Deprotonation and protonation

Fig. 6 examines the singly deprotonated form of DTPA, obtained by removing one proton from a carboxylic acid oxygen atom. Fig. 6a reveals that the removal induces a significant reorganization of the intramolecular hydrogen-bond network. The newly formed carboxylate group becomes a strong hydrogen-bond acceptor, engaging in two key interactions measuring 1.891 Å and 1.914 Å. These distances are substantially more compact than the neutral-state hydrogen bonds. Such change arises from the increased negative charge on the carboxylate oxygen, which enhances its ability to accept hydrogen bonds from neighboring carboxylic acid groups. Fig. 6b provides a CDD plot focused on the deprotonated carboxylate region, with orange dashed circles marking the primary sites of charge variation. The redistribution underscores the cooperative nature of the hydrogen-bond network: the negative charge is not confined to a single oxygen but is partially delocalized through the network of strong hydrogen bonds. Fig. 6c reports the frontier orbital energies of the singly deprotonated anion. The HOMO is calculated to locate at an elevated energy relative to the neutral molecule, while the LUMO shifts accordingly, resulting in a HOMO and LUMO of −1.633 ev, and 1.264 eV, respectively. These values represent a dramatic reduction of MO-gap from the neutral gap with value of 1.897 eV.

Fig. 7 examines the singly protonated form of DTPA, obtained by adding one proton to a carboxylic acid oxygen atom. Fig. 7a reveals that the addition induces a significant reorganization of the intramolecular hydrogen-bond network. The annotated distance O–H···O of 1.827 Å is substantially shorter than the neutral-state hydrogen bonds, indicating that the protonated species exhibits significantly strengthened hydrogen bonding. A second hydrogen bond is also resolved at 1.986 Å, further stabilizing the folded conformation. The result is a more rigidified molecular scaffold that may exhibit distinct electrochemical behavior compared to the neutral molecule. The isosurfaces in CDD plot (Fig. 7b) reveal a pronounced charge accumulation around the newly formed O–H bonds of the protonated group, confirming the localization of the positive charge. Meanwhile, the frontier orbital energies of the protonated cation in Fig. 7c exhibit a comparable MO-gap observed for the deprotonated species. In detail, the HOMO is calculated to locate at −8.664 eV, while the LUMO resides at −6.859 eV, yielding a gap of 1.805 eV. Such substantial narrowing comparing to neutral state suggests that protonation, similar to deprotonation, could render DTPA photoactive in the visible region—a critical consideration for its intended application as a photocatalyst component. Moreover, both the HOMO and LUMO are shifted downward relative to the neutral molecule, reflecting the stabilizing effect of the positive charge on all orbital energies.

3.4. Dimer interaction

Fig. 8 extends the analysis from isolated DTPA molecules to their dimeric assembly, providing insight into how DTPA molecules interact with one another. To identify the most stable configurations for the DTPA dimers, a comprehensive

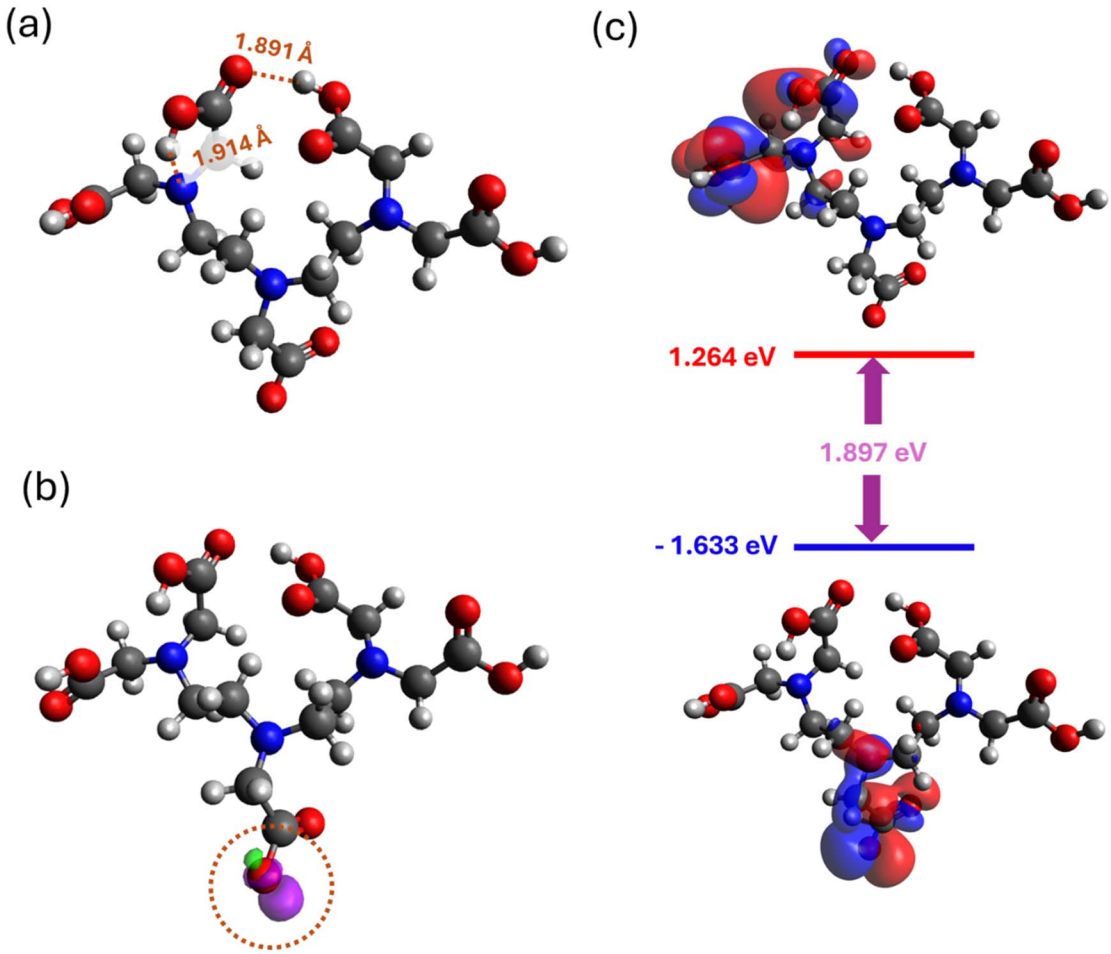

Fig. 6 Deprotonated form of DTPA after removal of one proton from a carboxylic oxygen atom. (a) Optimized molecular structure with selected hydrogen bond lengths (Å). (b) Vertical CDD plot of the deprotonated carboxylate group (orange dashed circle). (c) Calculated frontier orbital energies (HOMO and LUMO) and HOMO–LUMO gap of the singly deprotonated DTPA anion.

conformational search was conducted by considering over 10 initial orientations. These configurations accounted for diverse spatial arrangements, including various hydrogen-bonding motifs and electrostatic interactions between the monomeric units. The convergence of multiple initial guesses toward a consistent set of low-energy geometries provides confidence that the identified dimers represent the dominant species on the potential energy surface, characterized by a complex network of stabilizing intermolecular interactions.

Such intermolecular interactions are relevant not only for understanding the aggregation behavior of DTPA in solution or on surfaces but also for assessing the competitive binding when the molecule is adsorbed onto a typical substrate. Fig. 8a displays the optimized geometry of the DTPA dimer, revealing that two monomers associate through a network of intermolecular hydrogen bonds. The interaction is primarily mediated by the carboxylic acid groups, which engage in head-to-head O–H···O contacts between the two molecules. The dashed lines in the figure highlight these hydrogen bonds, which exhibit distances characteristic of moderately strong interactions. The dimer adopts a geometry that maximizes these contacts while minimizing steric repulsion, resulting in a compact, face-to-face arrangement. Fig. 8b provides a side view of the electrostatic potential surface mapped onto the dimer. The electrostatic complementarity is the driving force behind the dimerization, as it enables the formation of selective hydrogen bonds. The side view also reveals that the dimer interface is relatively planar, suggesting that DTPA molecules could potentially stack or form extended hydrogen-bonded networks in concentrated solutions or when immobilized on a surface.

3.5. Graphene interaction

Fig. 9 transitions from the molecular and dimeric analyses of DTPA to the hybrid system: the adsorption of DTPA onto graphene substrates. These configurations included various lateral displacements and rotations of the DTPA molecule relative to the pristine and defected (SW and V_1) regions. Full geometry optimizations revealed that the most stable configurations involve a synergistic interaction where the DTPA functional groups align with the high-reactivity zones of the topological

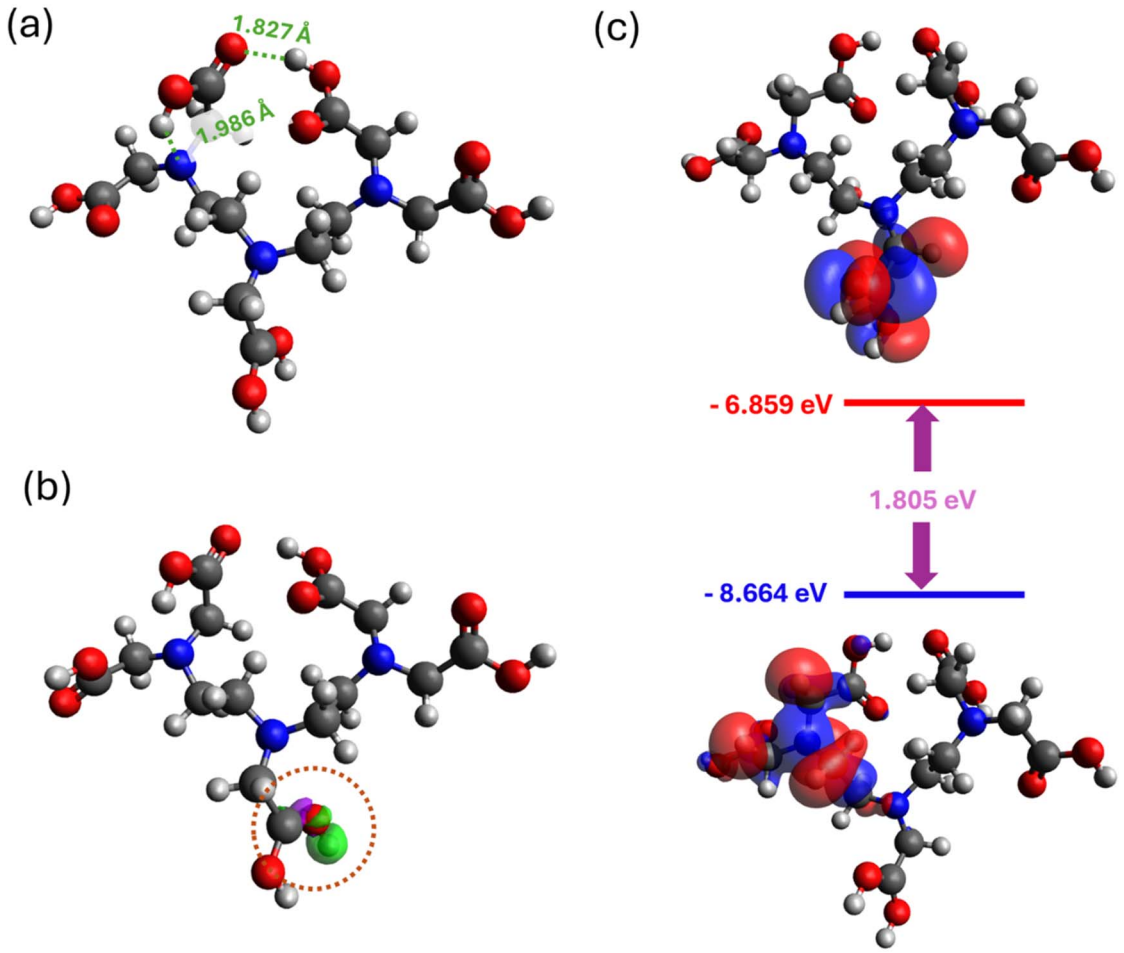

Fig. 7 Protonated form of DTPA after addition of one proton to a carboxylic oxygen atom. (a) Optimized molecular structure with selected intramolecular hydrogen bond lengths (Å). (b) Vertical CDD plot of the protonated carboxylate group (orange dashed circle). (c) Calculated frontier orbital energies (HOMO and LUMO) and HOMO–LUMO gap of the singly protonated DTPA cation.

defects. The figure systematically examines how the nature of the graphene support—specifically the presence and type of defects—influences the binding strength and geometry of DTPA. Spin-polarized calculations (Table S6) show that the isolated single-vacancy defect has a triplet ground state ($\langle S^2 \rangle = 2.02$), which is fully quenched upon DTPA adsorption, ruling

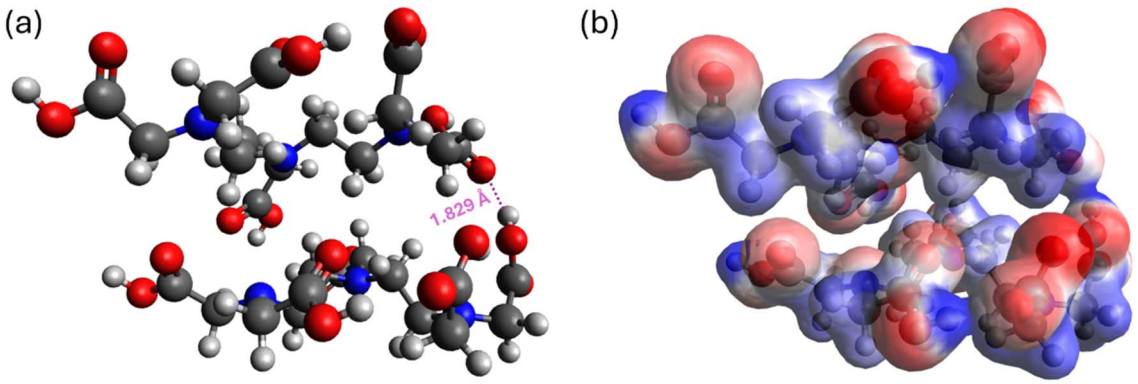

Fig. 8 Optimized dimer configuration of two DTPA molecules. (a) Interaction between two DTPA monomers *via* hydrogen bonds (dashed line). (b) Side view of the electrostatic potential surface showing regions of attractive electrostatic interaction between the carboxylic acid groups of the two monomers.

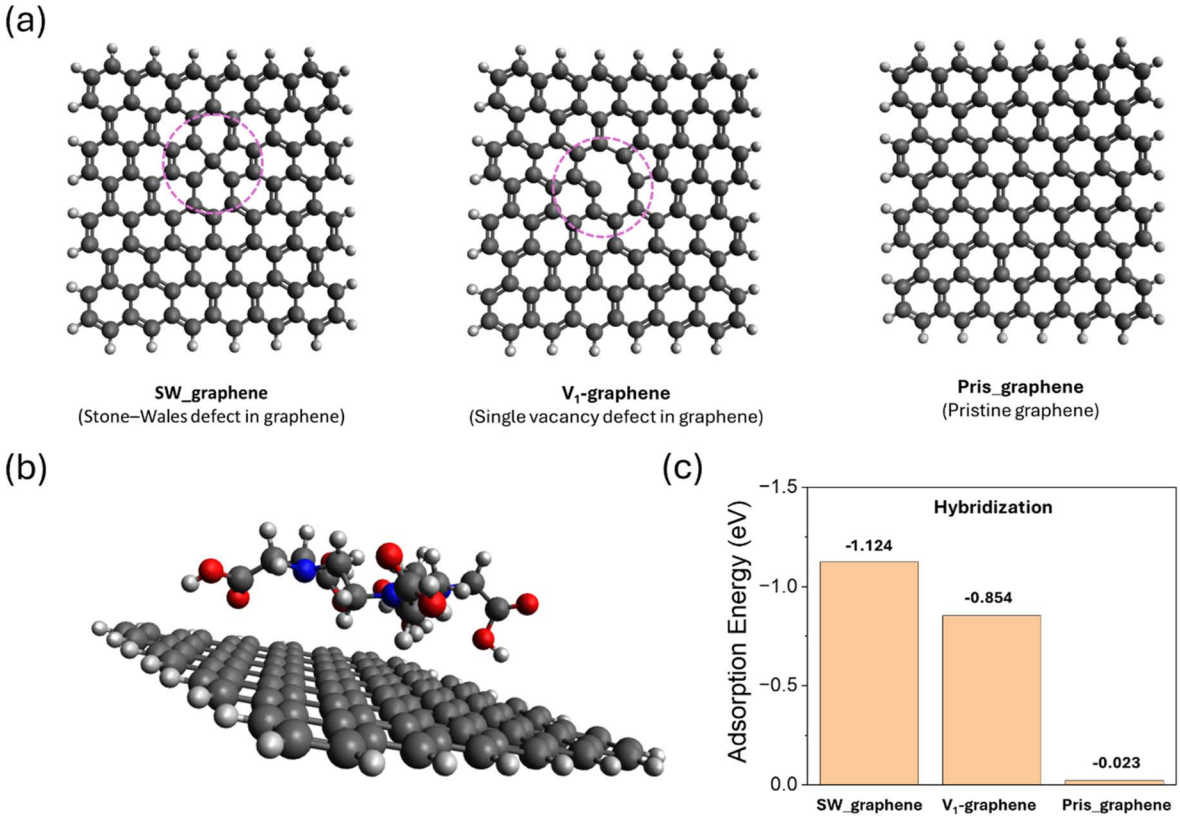

Fig. 9 Graphene substrates employed in the DFT calculations and the adsorption energy of DTPA. (a) Optimized structures of pristine graphene and two defected graphene models: Stone–Wales (SW) defect and single-vacancy (V_1) defect. (b) Representative geometry of DTPA adsorbed on studied graphene (side view). (c) Comparison of adsorption energies (E_{ads}) for DTPA on graphene. The values are given in eV and were calculated with dispersion correction.

out any spin-related artifacts in the computed adsorption energies. Fig. 9a establishes the structural diversity of the graphene substrates employed in this study. Pristine graphene serves as the baseline, representing an ideal, defect-free surface characterized by a uniform sp^2-carbon network. In contrast, the Stone–Wales defect introduces a topological rearrangement: a 90° rotation of a C–C bond converts four hexagons into two pentagons and two heptagons, creating a local strain field while preserving the atomic count. This defect is known to modify the electronic structure by introducing mid-gap states and altering the local reactivity. The single-vacancy (V_1) defect, formed by the removal of one carbon atom, creates a more substantial disruption: a dangling bond at the vacancy site induces a localized magnetic moment and significantly enhances the chemical reactivity of the surrounding carbon atoms. The purple dashed circles in Fig. 9a draw attention to these defect regions, underscoring that the subsequent adsorption behavior is governed not by the ideal graphene lattice but by these localized structural perturbations.

Fig. 9b provides a representative side-view of the adsorption geometry of DTPA on graphene surface. The molecule adopts a conformation that maximizes interfacial contacts while preserving its characteristic intramolecular hydrogen-bond network. Fig. 9c quantifies the strength of these interactions through the computed adsorption energies with dispersion correction. In detail, the SW-defect exhibits the most robust binding affinity for DTPA with an adsorption energy of −1.124 eV, which is significantly stronger than that of the single-vacancy (V_1) defect (−0.854 eV) and pristine graphene (−0.612 eV). This improved binding trend is in excellent agreement with recent theoretical investigation,[29] which demonstrated that the formation of heptagon–pentagon pairs in the Stone–Wales lattice, thereby facilitating stronger donor–acceptor interactions with organic ligands.[30] The values reveal a clear trend: adsorption on pristine graphene is the weakest, reflecting the relatively inert nature of the ideal sp^2 lattice, which primarily interacts through weak van der Waals forces.[31–33] The Stone–Wales defect leads to the highest adsorption energy, as the local strain and electronic redistribution create more favorable interaction sites.[34,35] The single-vacancy defect also enhances binding compared to pristine graphene, although its adsorption energy is slightly lower than that of the SW defect. Such observation may be attributed to the presence of undercoordinated carbon atoms at the vacancy site, which act as active centers for defect-induced dipole moments that enhance electrostatic interactions.[36–38] To assess finite-size effects, the adsorption energy of DTPA on SW-defected graphene was computed for clusters containing 103, 149, and 169

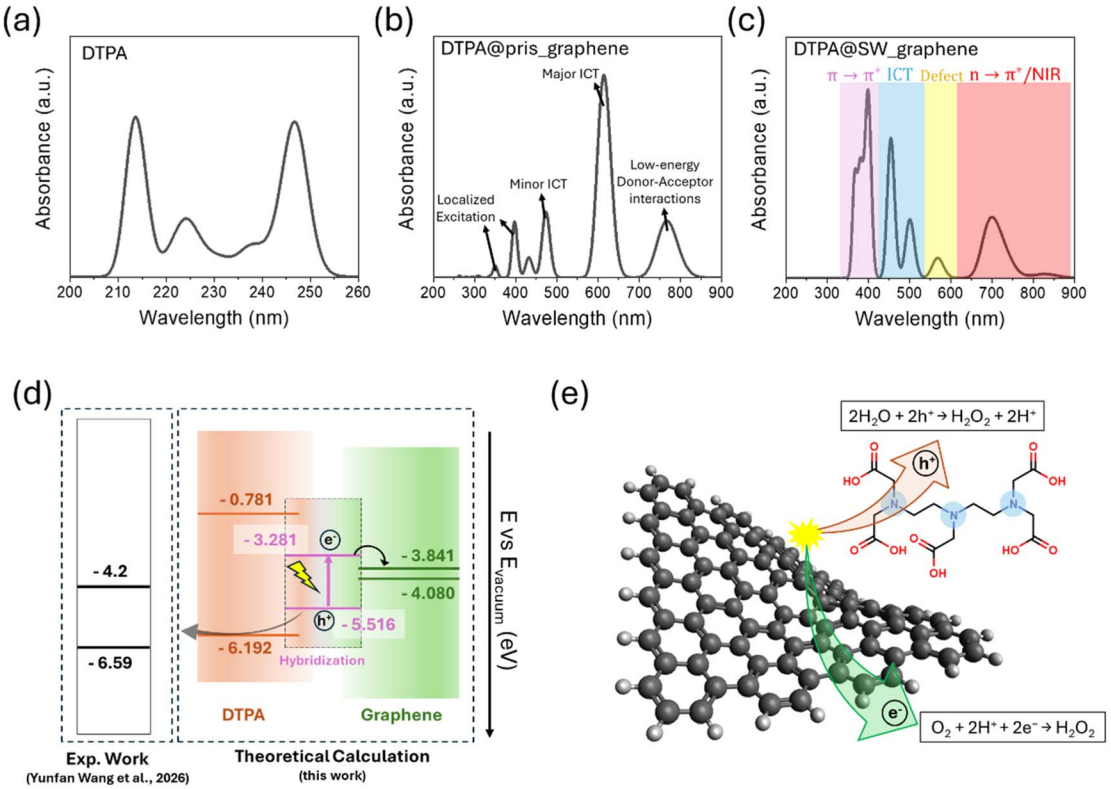

Fig. 10 (a–c) Simulated UV-Vis absorption spectra for isolated DTPA, DTPA@pristine graphene, and DTPA@SW-defected graphene in water. (d) Calculated energy level alignment between DTPA and graphene frontier orbitals, showing the hybridization-induced mid-gap states. (e) Proposed photocatalytic mechanism for H_2O_2 production, illustrating the synergistic electron–hole separation facilitated by the DTPA-graphene interface.

carbon atoms (see Fig. S3 and Table S7 in the SI). The energy difference between the smallest and largest clusters is 0.03 eV (≈2.6%), confirming typical convergence.

Obviously, Fig. 9 establishes a clear correlation between the defect chemistry of graphene and the adsorption strength of DTPA. The progression from pristine to V_1-defected to SW-defected graphene corresponds to an increasing propensity to immobilize the molecule, with the Stone–Wales defect emerging as the most promising substrate for creating a stable hybrid photocatalyst. This finding is particularly significant in light of the photocatalytic mechanism, where efficient charge separation requires intimate electronic coupling between DTPA and the graphene support. The strong adsorption on defected graphene not only ensures structural stability under operating conditions but also facilitates the alignment of frontier orbitals.

3.6. Propose mechanism for DTPA@graphene-based photocatalyst

Recent experimental advancements in carbon-based metal-free photocatalysts have proposed novel hybrid that comprises DTPA molecular active sites embedded in a semi-carbonized glucose-derived matrix and demonstrated its exceptional visible-light activity and stability.[20] This experimental work highlights the critical role of the semi-carbonized support in

Table 4 Frontier orbital energies (eV *vs.* vacuum) and corresponding one-electron redox potentials (*V vs.* NHE at pH 7) for isolated DTPA, SW-defected graphene, and the DTPA@SW-graphene hybrid[a]

Species	Orbital/level	Energy (eV)	Potential (V)	Role
Isolated DTPA	HOMO	−6.192	+1.752	Reference: strong oxidizer
SW-graphene	LUMO	−3.841	−0.599	Electron acceptor after photoexcitation
Hybrid	HOMO (hole localization site)	−5.516	+1.076	Oxidizes H_2O to H_2O_2
Hybrid	LUMO (excited electron)	−3.281	−1.159	Intermediate; electron transfers to graphene LUMO
Thermodynamic requirement	Water oxidation to H_2O_2	—	+1.35	$2H_2O \rightarrow H_2O_2 + 2H^+ + 2e^-$
Thermodynamic requirement	O_2 reduction to H_2O_2	—	+0.68	$O_2 + 2H^+ + 2e^- \rightarrow H_2O_2$

[a] The conversion uses $U_{NHE} = -(E_{vacuum} + 4.44)$. Thermodynamic requirements for the two half-reactions at pH 7.

enhancing charge extraction and overall photocatalytic efficiency. Motivated by these experimental observations, a possible mechanism of enhancement in photocatalytic of hybrid was proposed. Herein, the SW_defected graphene was served as a well-defined model for the semi-carbonized support toward defect-focused optical investigation.[39]

The optical properties and electronic transitions of DTPA, both in its isolated form and when anchored on graphene surfaces, were investigated using TD-DFT calculations in the aqueous phase (Fig. 10a–c). The isolated DTPA molecule (Fig. 10a) exhibits absorption exclusively in the ultraviolet region ($\lambda < 260$ nm), consistent with its large HOMO–LUMO gap. However, upon interaction with pristine graphene (Fig. 10b), the system displays a significant redshift, characterized by a major Interfacial Charge Transfer (ICT) peak at approximately 620 nm and a minor ICT transition near 480 nm. The introduction of lattice defects in the DTPA@SW_graphene model (Fig. 10c) further modulates the optical response, resulting in a dense manifold of transitions across the visible and near-infrared (NIR) spectra. Deconvolution of the absorption profile reveals that while $\pi \rightarrow \pi^*$ localized excitations dominate the UV-blue region, the synergistic coupling between DTPA and defected graphene sites facilitates broad visible-light harvesting through ICT and defect-mediated transitions (400–600 nm). Detailed excited-state parameters, including calculated excitation energies, maximum absorption wavelengths, oscillator strengths, and transition dipole moments for these systems, are systematically tabulated in Tables S8–S10 of the SI. These results confirm that the interfacial hybridization effectively lowers the energy barrier for electronic excitation, justifying the visible-light-driven photocatalytic activity observed experimentally.

Fig. 10 presents a proposed photocatalytic mechanism for the DTPA@SW_graphene hybrid, built upon the structural, electronic, and interfacial insights established in the preceding figures. Fig. 10d provides an energy level diagram that aligns the frontier orbitals of isolated DTPA with Stone–Wales defected graphene before and after hybridization. The left and right side of the diagram displays the calculated HOMO and LUMO energies of the isolated DTPA molecule and SW_graphene, respectively. Upon hybridization, the diagram illustrates a significant reorganization: the frontier orbitals of DTPA interact with the defect states of graphene, leading to a downward shift of the LUMO and an upward shift of the HOMO relative to their isolated positions. Most notably, the emergence of a smaller gap around 2.24 eV suggests that the hybrid becomes photoactive in the visible region, a critical requirement for an efficient photocatalyst. The hybridization facilitates the alignment of the LUMO with the graphene level, promoting efficient electron transfer from the photoexcited hybrid to the conductive graphene support.

The proposed photocatalytic mechanism for the DTPA@SW-graphene hybrid is illustrated in Fig. 10e. The thermodynamic feasibility of the dual-pathway H_2O_2 production is established through a site-specific hole localization mechanism. Under illumination, the hybrid absorbs visible light, generating an electron–hole pair. The photogenerated hole is localized on the DTPA moiety within the hybrid, with an oxidation potential of +1.076 V *vs.* NHE at pH 7 (see Table 4). This potential is only 0.27 V lower than the thermodynamic requirement for water oxidation to H_2O_2 (1.35 V), a small overpotential that is well within the typical error range of DFT (0.2–0.5 V) and can be overcome by the excess photon energy. Thus, the hybrid can drive the oxidation half-reaction: $2H_2O \rightarrow H_2O_2 + 2H^+ + 2e^-$. Concurrently, the photoexcited electron is spontaneously transferred from the hybrid LUMO (−1.159 V) to the LUMO of the SW-defected graphene (−0.599 V), which serves as an electron acceptor and transporter. The electron on graphene is sufficiently reducing to reduce O_2 to H_2O_2, as the required potential for $O_2 + 2H^+ + 2e^- \rightarrow H_2O_2$ is only +0.68 V *vs.* NHE, providing a large thermodynamic driving force ($\approx$1.28 eV). The spatial separation of the redox sites—oxidation on the DTPA molecule and reduction on graphene — minimizes charge recombination.

These theoretical predictions are strongly supported by the experimental study of Wang *et al.*,[20] which reported strong stability, efficient charge separation, and two-electron, two-proton pathways for both water oxidation and oxygen reduction (electron transfer number $\approx$2.5 from RRDE). The calculated strong adsorption on SW-defected graphene (Section 3.5) rationalizes the enhanced charge extraction and prolonged carrier lifetime observed in that work. The synergy between the deep-potential holes in DTPA and the electron-shuttling capability of the defected graphene matrix, as evidenced by Transient Photovoltage (TPV) measurements, confirms the high-efficiency, visible-light-driven H_2O_2 synthesis enabled by this molecular-carbon architecture.

4. Conclusion

In this study, a comprehensive DFT investigation was performed to evaluate the structural, electronic, and interfacial properties of diethylenetriaminepentaacetic acid (DTPA) and its hybrid with defected graphene for photocatalytic applications. The calculations reveal that isolated DTPA possesses a wide intrinsic band gap of 5.411 eV, with a distinct spatial separation of redox-active sites: holes localize on the tertiary amine–carboxylate core, while electrons reside on carbonyl oxygen atoms. This partitioning is fundamentally preserved across radical states and is further modulated by protonation or deprotonation. Upon adsorption onto defected graphene substrates, particularly the Stone–Wales (SW) defect, strong binding energies and favorable frontier orbital alignment substantially reduce the effective band gap, rendering the hybrid photoactive under visible light. A photocatalytic mechanism is proposed, wherein DTPA serves as the molecular photoactive center and defected graphene functions as an electron transporter and charge separator. This work establishes a rational foundation for the design of molecular-carbon hybrid photocatalysts. Future studies will focus on exploring the influence of different defect types, solvent environments, and co-catalyst integration to further optimize charge transfer kinetics and photocatalytic efficiency.

Author contributions

The manuscript was written through the contributions of all authors. All authors have approved the final version of the manuscript.

Conflicts of interest

The authors declare that they have no known competing financial interests or personal relationships that could have appeared to influence the work reported in this paper.

Data availability

Data will be made available on request. The datasets generated during and/or analyzed during the current study are available from the corresponding author upon reasonable request.

Supplementary information: SOMO/LUMO of radical ionization; convergence test for different size of graphene in hybrid; spin properties, electronic properties, and transition properties of ionized and hybrid forms. See DOI: https://doi.org/10.1039/d6ra02766k.

Acknowledgements

This research was conducted at Van Lang University (VLU) and Ton Duc Thang University (TDTU), where essential facilities and resources were provided. No additional support was received.

References

1 I. V Pylypchuk, D. Kołodyńska and P. P. Gorbyk, *Sep. Sci. Technol.*, 2018, **53**, 1006–1016.
2 T. Wu, L. Sun, F. Xu and D. Cai, *J. Mater. Sci. Technol.*, 2018, **34**, 2384–2391.
3 R. D. Hancock and A. E. Martell, *Chem. Rev.*, 1989, **89**, 1875–1914.
4 A. E. Martell and R. D. Hancock, *Metal Complexes in Aqueous Solutions*, Springer Science & Business Media, 2013.
5 G. Anderegg, F. Arnaud-Neu, R. Delgado, J. Felcman and K. Popov, *Pure Appl. Chem.*, 2005, **77**, 1445–1495.
6 S. Chaves, R. Delgado and J. J. R. F. Da Silva, *Talanta*, 1992, **39**, 249–254.
7 R. M. Smith and A. E. Martell, *Critical stability constants: second supplement*, Springer, 1989, vol. 6.
8 S. Leguay, T. Vercouter, S. Topin, J. Aupiais, D. Guillaumont, M. Miguirditchian, P. Moisy and C. Le Naour, *Inorg. Chem.*, 2012, **51**, 12638–12649.
9 K. L. Nash, D. Brigham, T. C. Shehee and A. Martin, *Dalton Trans.*, 2012, **41**, 14547–14556.
10 P. Modiba, M. Matoetoe and A. M. Crouch, *Electrochim. Acta*, 2013, **94**, 336–343.
11 S. Fukuda, *Curr. Med. Chem.*, 2005, **12**, 2765–2770.
12 G. N. Stradling, *J. Alloys Compd.*, 1998, **271**, 72–77.
13 P. Caravan, J. J. Ellison, T. J. McMurry and R. B. Lauffer, *Chem. Rev.*, 1999, **99**, 2293–2352.
14 M. Bottrill, L. Kwok and N. J. Long, *Chem. Soc. Rev.*, 2006, **35**, 557–571.
15 R. L. Sheppard, *Metal Chelates of Ethylenediaminetetraacetic Acid: Characterization and Quantitation in Human Plasma and Urine and Environmental Waters by Capillary Electrophoresis-Ion Spray Tandem Mass Spectrometry*, Cornell University, 1997.
16 L. Wachowski, J. W. Sobczak and M. Hofman, *Appl. Surf. Sci.*, 2007, **253**, 4456–4461.
17 T. Wu, L. Sun, F. Xu and D. Cai, *J. Mater. Sci. Technol.*, 2018, **34**, 2384–2391.
18 M. Eddaoudi, J. Kim, N. Rosi, D. Vodak, J. Wachter, M. O'Keeffe and O. M. Yaghi, *Science*, 2002, **295**, 469–472.
19 D. Maspoch, D. Ruiz-Molina and J. Veciana, *Chem. Soc. Rev.*, 2007, **36**, 770–818.
20 Y. Wang, F. Liao, H. Xiang, T. Shi, J. Wang, Z. Li, H. Huang, H. Wu, Y. Liu and Z. Kang, *Carbon*, 2026, 121272.
21 T. A. Kaden, in *Host Guest Complex Chemistry III*, Springer, 2005, pp. 157–179.
22 H. W. Kim, M. B. Ross, N. Kornienko, L. Zhang, J. Guo, P. Yang and B. D. McCloskey, *Nat. Catal.*, 2018, **1**, 282–290.
23 S. C. Ameta, R. C. Ameta, M. Bala and T. D. Dubey, *J. Chim. Phys.*, 1991, **88**, 191–199.
24 X. Yuan, Q. Zhou, Y. Chen, H.-J. Yang, Q. Jiang, J. Hu and C.-Y. Guo, *C*, 2024, **10**, 62.
25 S. V Badalov, R. Wilhelm and W. G. Schmidt, *J. Comput. Chem.*, 2020, **41**, 1921–1930.
26 F. Neese, *Wiley Interdiscip. Rev. Comput. Mol. Sci.*, 2012, **2**, 73–78.
27 F. Neese, F. Wennmohs, U. Becker and C. Riplinger, *J. Chem. Phys.*, 2020, **152**, 224108.
28 F. Neese, *Wiley Interdiscip. Rev. Comput. Mol. Sci.*, 2018, **8**, e1327.
29 A. Z. Jovanović, A. S. Dobrota, N. V Skorodumova and I. A. Pašti, *FlatChem*, 2023, **42**, 100573.
30 A. Z. Jovanović, A. S. Dobrota, N. V Skorodumova and I. A. Pašti, *FlatChem*, 2023, **42**, 100573.
31 X. Li, J. Yu, S. Wageh, A. A. Al-Ghamdi and J. Xie, *Small*, 2016, **12**, 6640–6696.
32 A. K. Geim and K. S. Novoselov, *Nat. Mater.*, 2007, **6**, 183–191.
33 C. N. R. Rao, K. Biswas, K. S. Subrahmanyam and A. Govindaraj, *J. Mater. Chem.*, 2009, **19**, 2457–2469.
34 S. K. Tiwari, S. K. Pandey, R. Pandey, N. Wang, M. Bystrzejewski, Y. K. Mishra and Y. Zhu, *Small*, 2023, **19**, 2303340.
35 J. Ma, D. Alfè, A. Michaelides and E. Wang, *Phys. Rev. B*, 2009, **80**, 033407.
36 J. J. Palacios, J. Fernández-Rossier and L. Brey, *Phys. Rev. B*, 2008, **77**, 195428.
37 F. Ducastelle, *Phys. Rev. B*, 2013, **88**, 075413.
38 E. Zaminpayma, M. E. Razavi and P. Nayebi, *Appl. Surf. Sci.*, 2017, **414**, 101–106.
39 W. Liu, Y. Han, M. Liu, L. Chen and J. Xu, *RSC Adv.*, 2023, **13**, 16232–16240.